# Reactor-scale Modeling and Control for MOCVD of YBCO High Temperature Superconductors

Application Notes: 1999

**SC Solutions, Inc.**
1261 Oakmead Pkwy
Sunnyvale, CA 94085
http://www.scsolutions.com

**Abstract:**

This paper details a systematic methodology for concurrent development of reactor-scale physical model and model-based process control development for metal-organic chemical vapor deposition (MOCVD). The example used for illustrating the approach is the deposition of yttrium-barium-copper oxide ($YBa_2Cu_3O_{7-x}$ or YBCO) thin films with high temperature superconducting (HTS) properties. Information about the gas-phase chemical mechanisms, obtained from experimental data in the literature, is used in the reactor-scale transport and kinetics model developed using the CFD-ACE™ software package. These models were used to design model-based controllers for desired deposition rate, and for uniformity of deposition rate and stoichiometry within wafer. These simulation tools and the results obtained from the studies provide a clearer understanding of the chemical mechanism, species transport, and film growth. This understanding enables design and implementation of optimized controllers that meet both process specifications as well as run-to-run repeatability, which are essential for large-scale production.

## 1 Introduction

As a technique for fabrication of HTS films, MOCVD offers the potential for growth under highly oxidizing conditions, for large area deposition, and high throughput. However, the process is highly complex, involving flow, heat transfer, and gas-phase and surface chemical kinetics at high temperatures [1,2]. Discussions on the more specific topic of MOCVD of high-$T_c$ HTS are in review papers [3-5], and in experimental results in the literature, e.g., [6,7].

The decomposition reactions of the precursors are crucial to MOCVD. Typical precursors for the growth of $YBa_2Cu_3O_{7-x}$ films are β-diketonates, e.g., $Ba(dpm)_2$ (dpm=3D dipivaloylmethanate) or $Ba(hfa)_2$=$B_7$tet (hfa=3D hexafluoroacetylacetonate, tet=3D tetraglyme). These precursors are typically difficult to transport and their decomposition mechanisms are poorly characterized. The current understanding of MOCVD of HTS films is limited to conditions leading to mass transport or kinetically limited growth regimes. Semi-empirical models based on assumptions of a few gas-phase reaction steps followed by overall surface

reactions have been proposed, but the chemical mechanisms underlying MOCVD is not understood [1].

Reactor scale transport models were developed for a horizontal MOCVD reactor using CFD-ACE™ [8], a multi-physics simulation and modeling package popular in the semiconductor industry. The model includes chemical kinetics and species transport to the wafer surface and calculates deposition rates and film thickness uniformity of YBCO as a function of growth conditions. The YBCO deposition rates obtained from these simulations are comparable to those published in the literature. Sensitivity calculations using this model were used for run-to-run controller design. A general control structure was developed for MOCVD reactor control systems. An innovative run-to-run controller scheme was developed that enables efficient convergence to the desired stoichiometry region for MOCVD systems using a multi-step process control method. A standard run is performed and performance measures are determined using ex-situ metrology. The run-to-run control iterations are then run on the virtual reactor model to suggest control perturbations for the next actual run to reach the desired stoichiometry region.

## 2 MOCVD Reactor Model

In order to link the gas phase chemistry information obtained from the previous section to YBCO deposition on the wafer, it is necessary to develop a reactor-scale model. This section describes such a model that solves the coupled flow, heat and species transport problem, and includes gas phase chemistry. A static response surface (input-output) model is then obtained from this detailed model for use in run-to-run control.

### 2.1 Description of the MOCVD system

A commercial, horizontal-flow, hot wall, quartz reactor (Thomas Swan) was used for reactor-scale transport and kinetics modeling. The system is equipped with independent evaporators contained in separate ovens to allow for evaporation of precursors with low vapor pressure at a maximum temperature 250$^{o}$C. The gas lines from the evaporators feed into a common temperature-controlled gas manifold that mixes the precursors and delivers them to the reactor. The precursor concentration in the gas entering the chamber is controlled by real-time, closed-loop feedback control using gas sensors. Actuation is achieved by adjusting one or more of the following process variables: the evaporator pressure, evaporator temperature, and the flow rate of carrier gas. The wafer is heated by infrared lamps that are grouped into three zones to permit susceptor temperature control using a thermocouple for each zone. Rotation of the substrates is used to improve the homogeneity.

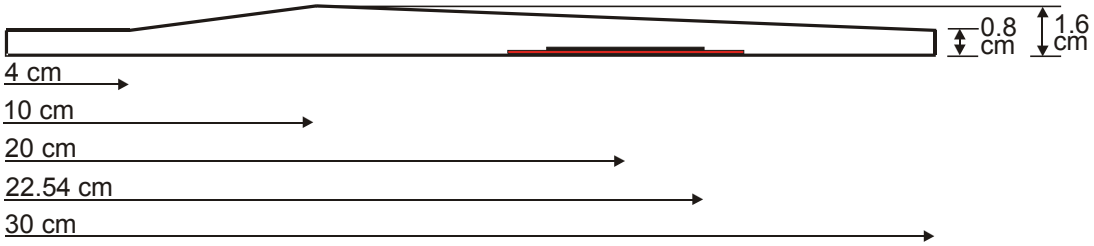


**Figure 1.** Schematic of STI's Thomas Swan MOCVD reactor.

For this study, a two-dimensional approximation of the chamber geometry was considered sufficient. The reactor is infinite in the transverse direction and is shown in Figure 3. While the reactor can accommodate up to seven wafers, this study considers a single wafer located with its center of the wafer of diameter 2" is located 20 cm from the left end of the reactor through which the gas mixture enters. The ceiling of the reactor slopes downward in order to compensate for species depletion and improve deposition uniformity along the wafer. Reducing the vertical distance in approximate proportion to species depletion can keep the species concentration gradients in the vertical direction (and hence, species flux towards the wafer surface) almost unchanged.

## 2.2 Finite-volume Physical Model of CVD Reactor

Figure 4 shows the structured mesh for the finite-volume CFD-ACE™ model constructed for the above reactor, magnified five times in the vertical direction for clarity. The mesh consists of 574 (14×41) cells which were found to be sufficient for obtaining a convergent solution. The model consists of a mass conservation equation, momentum conservation equations, the energy balance equation, species diffusion equations, and seven gas-phase reactions described next. Most of these equations are strongly coupled nonlinear partial differential equations. The above transport equations are solved using a control-volume approach [8]. In this solution, a first-order upwind scheme was used for the convective fluxes. CFD-ACE™ uses a pressure-based approach to solving the Navier-Stokes equations in which the continuity equation is used to recast these three equations is terms of pressure. This solution used the SIMPLEC method, a variation of the well-established SIMPLE algorithm [9].

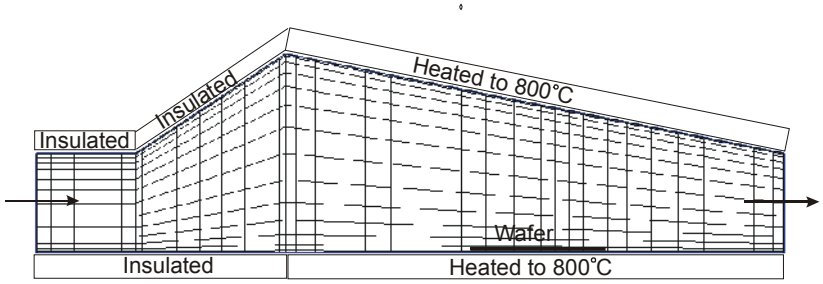


**Figure 2.** Mesh for numerical solution using CFD-ACE, clustered near the walls. For clarity, the vertical dimensions are magnified five times the horizontal dimensions.

For chemistry, we have used one-step global mechanisms for precursor decomposition. For $Cu(dpm)_2$, the kinetic rate constants were obtained as described in the previous section while rate

constants for the other two precursor decomposition were obtained from the literature [10]. The overall mechanism consists of seven gas phase reactions:

$$\begin{aligned}
Y(dpm)_3 + O_2 &\rightarrow Y + 3\,(dpm) + O_2 \\
Y(dpm)_3 &\rightarrow Y + 3\,(dpm) \\
Cu(dpm)_2 &\rightarrow Cu + 2\,(dpm) \\
Ba(dpm)_2 &\rightarrow Ba + 2\,(dpm) \\
4\,Y + 3\,O_2 &\rightarrow 2Y_2O_3 \qquad (2) \\
2\,Ba + O_2 &\rightarrow 2BaO \\
2\,Cu + O_2 &\rightarrow 2CuO
\end{aligned}$$

The last three oxidation reactions in Equation set (2) are relatively fast. The Arrhenius rate constants for the first four reactions are shown in Table 1. The oxides produced in the gas phase reaction diffuse to the surface and their deposition was modeled using sticking coefficients, assumed to be $5.0\times10^{-4}$ for all three oxides [11]. The transport properties of some of the species were calculated using Lennard-Jones parameters. For the oxides, data on melting point temperatures, $T_m$, and the liquid molar volume, $V_b$, were used to calculate the parameters using the following correlations from the literature [12].

$$\varepsilon/k = 1.92\,T_m ; \sigma = 1.166\,V_b^{1/3}$$

**Table 1:** Arrhenius rate coefficients for decomposition reactions

| Reaction | *A* | $E_a/R$ (K) |
|---|---|---|
| $Y(dpm)_3 + O_2 \rightarrow Y + 3\,(dpm) + O_2$ | $5.9\times10^{-12}$ $m^3$/kg-mole.s | 13590.4 |
| $Y(dpm)_3 \rightarrow Y + 3\,(dpm)$ | $2.2\times10^{9}$ $s^{-1}$ | 17264.9 |
| $Cu(dpm)_2 \rightarrow Cu + 2\,(dpm)$ | $1.0\times10^{13}$ $s^{-1}$ | 13620.6 |
| $Ba(dpm)_2 \rightarrow Ba + 2\,(dpm)$ | $2.2\times10^{9}$ $s^{-1}$ | 17264.9 |

For the precursors, melting point data was used to calculate $\varepsilon/k$. The collision diameter, $\sigma$, was calculated from data on $\sigma_{ij}$ for precursor and oxygen [13]. Since data for $Cu(acac)_2$ is reported, we use these values for $Cu(dpm)_2$ for lack of more accurate values of the transport properties. Finally, the values of Lennard-Jones parameters used in the model are shown in Table 3.

The oxidation reactions are instantaneous while the decomposition reactions are finite-rate, making the system of equations very stiff. We decided to simplify the model by eliminating the four oxidation reactions from the mechanism used in the model. The metallic atoms are assigned the transport properties of the oxides, which then diffuse to the surface. Because the mole fractions of the precursors are very small (of the order of tens of ppm), the excess oxygen not used up in oxide formation are also very small, and its effect on the flow and temperature fields is insignificant. This simplification halved the computational time without any loss in accuracy.

Because the temperature gradients inside the hot-wall reactor are small, thermodiffusion was found to be negligible. Stefan-Maxwell conservation for multi-species diffusion was used in the calculations. A typical simulation converged within 2000 iterations in approximately fifteen minutes of CPU time on a Pentium (800 MHz) desktop computer.

Results are shown below for the following representative steady-state operating conditions [11]. The precursors are well-mixed with oxygen, nitrogen, and argon and enter the reactor at 10 Torr at a velocity of 2 m/s and temperature of 513K. The inlet mass fractions are: $O_2$=0.456, $N_2$=0.422, Ar=0.114, $Y(dpm)_3=9.32\times10^{-4}$, $Ba(dpm)_2=1.57\times10^{-3}$, $Cu(dpm)_2=5.02\times10^{-3}$. The wall of the plenum is insulated up to the highest point of the chamber (10 cm from the entry port). The remaining 20 cm of the reactor are heated radiantly so that both the top and bottom surfaces are kept at 850°C (1073K). Although the 2" diameter wafer is centered 20 cm from the entry port, deposition occurs along the entire length of the heated lower surface. Figure 5 shows the flow velocity vectors with the shading scheme showing the magnitude (speed). The flow speeds up considerably as it gets hotter. Figure 6 shows the temperature profiles in the direction of flow, and in the vertical direction. The gas heats up quickly as it passes over the heated section, and its temperature is quite close to the surface temperature. The temperature profile in the vertical direction is very uniform, and the heat transfer in the gas is conduction dominated.

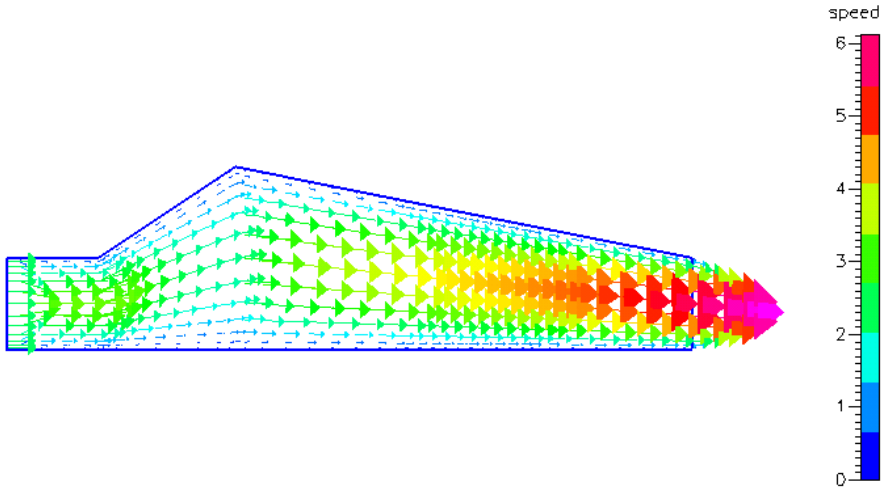


**Figure 3.** Velocity distribution in MOCVD reactor.

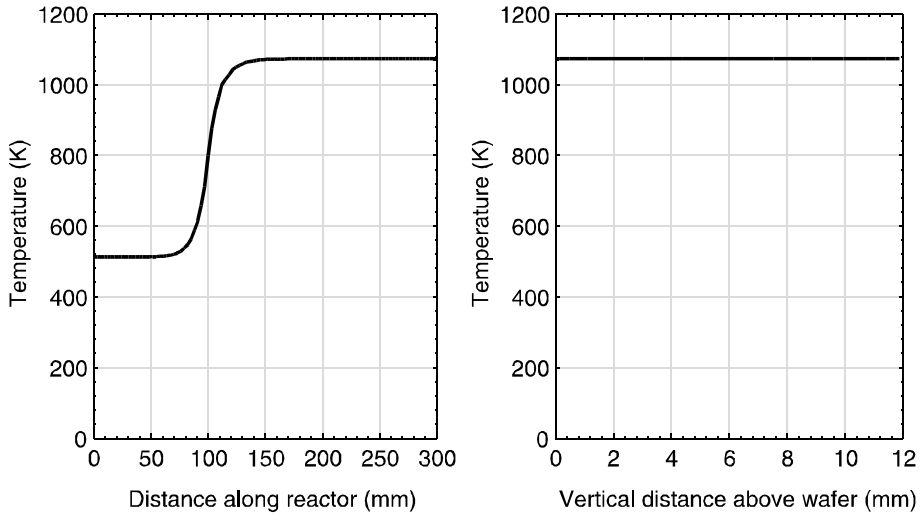


**Figure 4.** (a) Gas temperature profile along the length of the MOCVD reactor 5 mm above the wafer (b) Gas temperature profile in the vertical direction above the center of the wafer.

In this model, YBCO deposition rate is calculated by adding the deposition rates of each of the three individual oxides determined from separate simulations. Figure 7 shows the precursor concentrations along the reactor length 5 mm above the wafer surface. It is seen that the precursors decompose very quickly as they enter the heated region. Figure 8(a) shows the oxide mole concentrations in the flow direction 5 mm above the wafer. The oxide concentration decreases along the flow direction due to depletion. Figure 8(b) shows the concentration gradient in the vertical direction at the center of the wafer. The gradient of CuO is significantly higher than the other two oxides indicating a higher flux arriving at the surface. Since the sticking coefficients for the three oxides are all taken as 0.05, the mass deposition rate of CuO is also the highest.

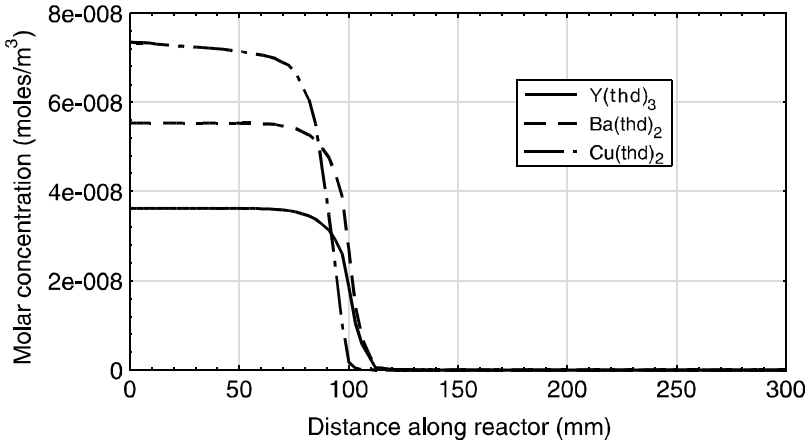


**Figure 7.** Spatial profiles of precursor mole fractions along the reactor length, 5 mm above the wafer.

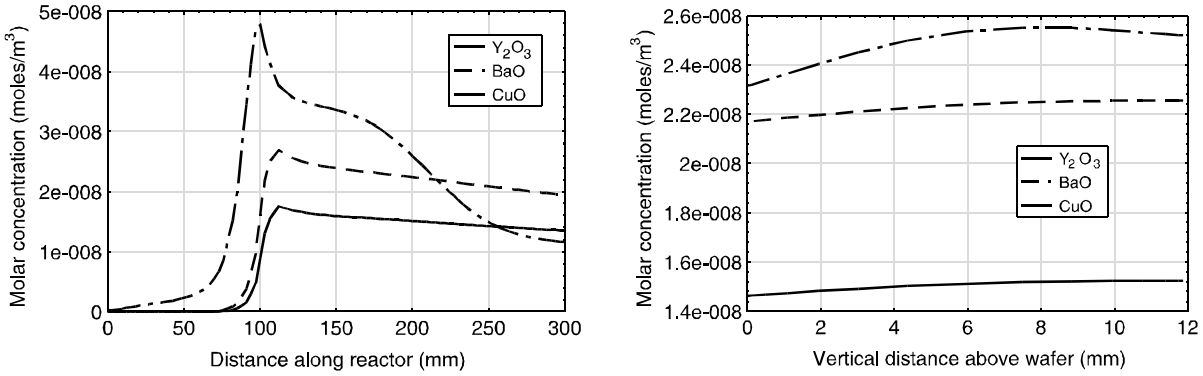


(a) (b)

**Figure 8. (a)** Oxide mole fraction profiles along the length of the MOCVD reactor 5 mm above the wafer. **(b)** Oxide mole fraction profiles in the vertical direction above the center of the wafer.

Figure 9(a) shows the deposition rate along the diameter of a static 2" (5 cm) wafer, while Figure 9(b) shows the sum of these three deposition rates resulting in a YBCO deposition rate of 44 Å/min averaged along the wafer. For comparison, the deposition rates for YBCO MOCVD reported in the literature range from 30 Å/min to 150 Å/min [3-5]. The significant deposition non-uniformity (~ 16%) shown in Figure 9 can be improved by radial averaging of the film deposition achieved by rotating the wafer with period of rotation that is much smaller than the deposition time. In this case, the deposition times are in the order of tens of minutes and hence the rotational speed may be as small as 10 rpm. Figure 10 shows the deposition profile with wafer rotation. Since the deposition profile along the static wafer is linear for all three oxides (Figure 9), rotating the wafer leads to excellent uniformity (less than 1% non-uniformity).

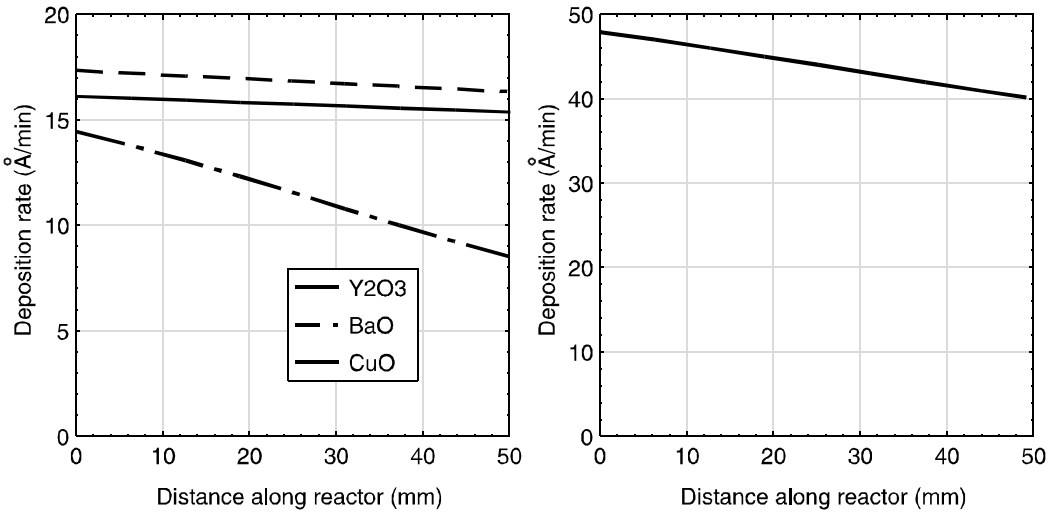


(a) (b)

**Figure 9.** Deposition rates in Å/min, when the wafer is not rotated. (a) Rates for individual oxides, (b) total deposition rate for all three oxides.

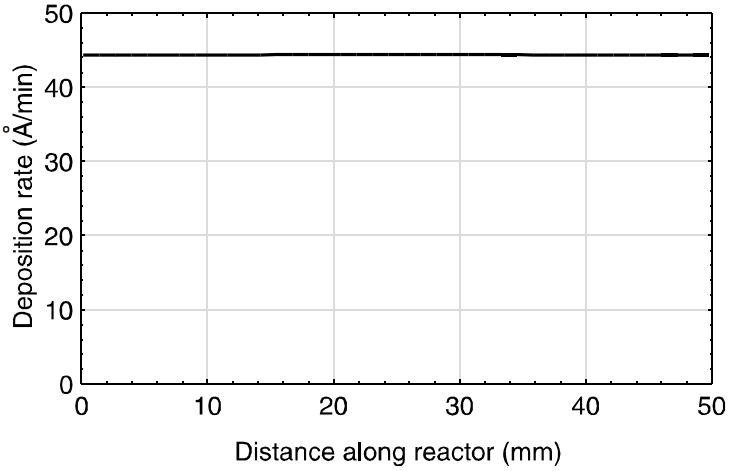


**Figure 10.** YBCO deposition rates in Å/min with wafer rotation.

It is important to note that the non-uniformity can be affected by surface chemistry. In a transport-limited case with a high sticking coefficient of 0.5, the deposition profile along a static wafer would be non-linear as shown in Figure 11(a). The precursor concentrations for these calculations were suitably reduced to keep the YBCO deposition rate close to that of the previous case. Figure 11(b) shows that wafer rotation in this case will produce a bowl-shaped profile with non-uniformity higher than 13% even within a the small 2" wafer. Figure 12 shows the stoichiometry of YBCO thin film across the wafer as expressed in ratios of yttrium oxide moles to the moles of the other two oxides at a given point on the wafer. In general, its is desirable to have the $BaO/Y_2O_3$ ratio slightly below two, and the $CuO/Y_2O_3$ ratio slightly above three [3]. Run-to-run control, described in the next section, is used to adjust the inputs to restrict the stoichiometry and deposition rates in the desired performance region.

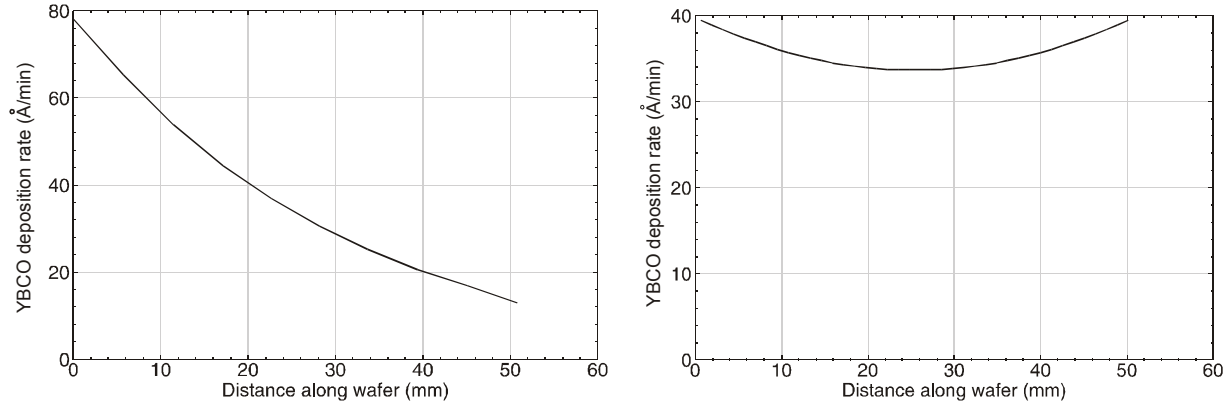


**Figure 11.** YBCO deposition rates (Å/min) using a sticking coefficient of 0.5, (a) without wafer rotation, (b) with wafer rotation.

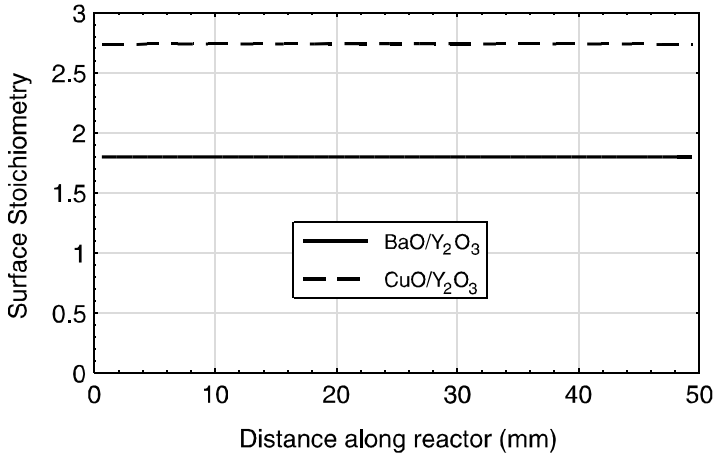


**Figure 12.** Oxide stoichiometry at the wafer surface expressed as ratios of yttrium (and barium) atoms to copper atoms.

The primary limitation of this reactor-scale model is lack of knowledge of the surface chemistry, which affects both growth rate and within-wafer uniformity. Additionally, susceptor temperature non-uniformities will reduce deposition uniformity. However, the main purpose of the model, which is to illustrate a methodology for linking fundamental chemistry to model-based control for manufacturing, has been satisfactorily achieved. Higher order models with more accurate chemistry can replace the current model in the future.

## 3 Model-Based Control for HTS MOCVD

The final step in this integrated methodology is to use the information obtained from *ab initio* DFT calculations, and the reactor-scale transport and chemistry model, towards model-based control that helps improve the manufacturing process. This section describes the overall control hierarchy, and examines the run-to-run control strategy more closely.

### 3.1 Control Objectives and the Control Problem

The primary control objective is to obtain a uniformly distributed YBCO deposition of desired thickness and stoichiometry on a wafer, with little variation from wafer-to-wafer. Thickness non-uniformity is primarily caused by species depletion as well as by temperature non-uniformity on the wafer. Temperature non-uniformity is particularly an issue at lower temperatures, closer to the kinetic limit. Stoichiometry non-uniformity is primarily caused by unequal gas-phase diffusivities of the three oxides, and any fluctuations or drifts in the precursor flows. Rotating the wafer improves thickness uniformity, but results in a concave profile with the minimum thickness at the center of the wafer.

The inputs available for deposition control are the flow rate and/or pressure of the carrier gas, the temperature of the susceptor, and the concentration of the precursor gases (by controlling the evaporator temperature and pressure). The outputs that are measured are the flow rates of carrier gas (*in-situ*), susceptor temperatures measured using thermocouples (*in-situ*), and the deposition thickness (*ex-situ*). The wafer temperature may or may not be measured using a pyrometer, or has to be deduced from the susceptor temperature. The expected sources of noise and

disturbances include measurement noise on all measurements, random fluctuations in flow rate, random fluctuations in precursor concentration, and drifts in wafer and susceptor temperatures. The control problem is to obtain deposition thickness with desired deposition uniformity using the available control inputs and measured outputs, in the face of the expected noise and disturbances. The physical model described in the previous section approximates the static global behavior of the MOCVD reactor, and is used in the controller design.

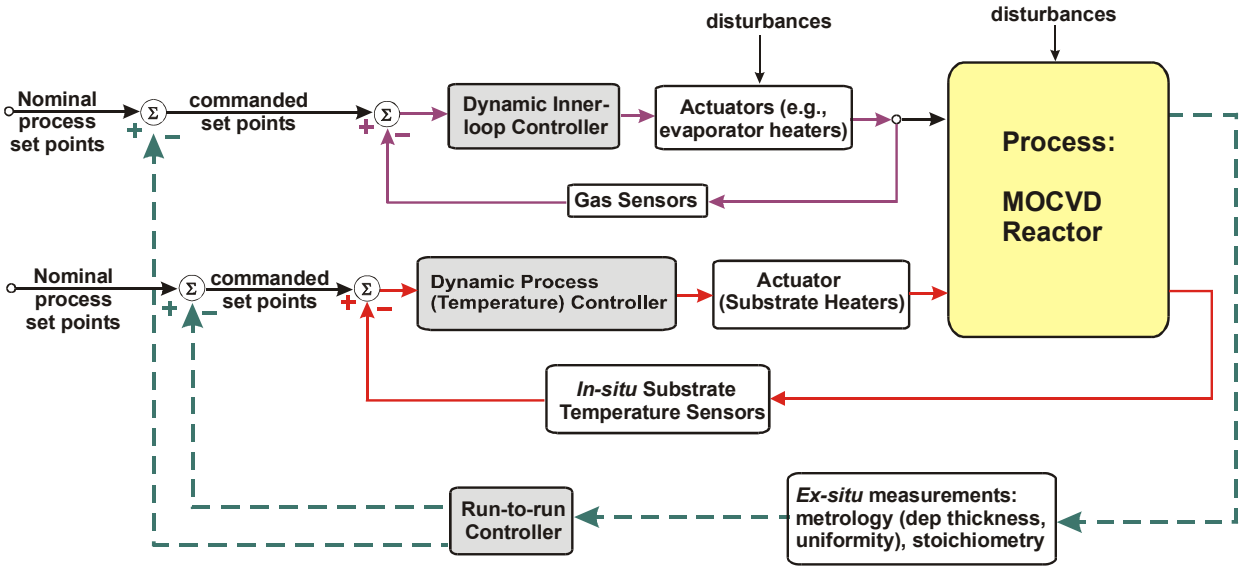


**Figure 13.** Schematic of control structure for MOCVD of HTS thin films**.**

### 3.2 Overall Control Strategy

The control inputs include flow rates of precursors, oxidizer (oxygen), and carrier gas (argon), and the temperature set-points for the susceptor temperature controller. Since the deposition process is slow as a function of control inputs, it can be considered as a static system. Therefore, there may be no need for a dynamic controller that tries to control deposition directly from the manipulated inputs. Instead, the film with desired thickness and stoichiometry is grown by regulating the inputs at a desired (nominal) operating point. However, all disturbances at the evaporator and reactor level are dynamic, which implies that dynamic "slave" controllers are needed locally to obtain tight regulation at the desired operating points. The proposed control hierarchy is shown in Figure 13. The control structure shows both dynamic control of precursor flow and susceptor temperature using *in-situ* sensing as well as a run-to-run control employing *ex-situ* sensors. The evaporators are controlled by local (inner-loop) controllers, there are *in-situ* temperature sensors measuring substrate temperature corresponding to substrate (segmented) heaters, and metrology is employed to measure the outputs, which are the wafer properties of interest (deposition thickness and uniformity, stoichiometry).

It is expected that integral control and (notch) filtering possibly extended with some phase compensation will give tight regulation for precursor flow and temperature. One would use low-order dynamic heat transfer models of the evaporators and the chambers that relate measured outputs to manipulated inputs and disturbances/noise. These inner-loop dynamic controllers are not discussed here.

Run-to-run control has been shown to be an excellent means to achieve desired film properties, for example, in rapid thermal oxidation processes [14]. Here, the values of the nominal operating set-points (called recipe variables) are adjusted after one run of the process based on *ex-situ* measurements of wafer properties before processing the next wafer. The CFD-ACE™ static model described in the previous section relates the manipulated inputs to the measured deposition thickness and stoichiometry, and can be used to generate the static model for the run-to-run controller design. Since the model does not capture chemistry as a function of temperature, we use only the precursor concentrations as inputs. The model is run after varying each precursor concentration (i.e., input or recipe variable) while keeping the others unchanged at the nominal values.
For small variations, a single perturbation from the nominal value per recipe variable is sufficient to create the model. For larger variations, non-linear behavior may need to be taken into account by calculating deposition thickness and uniformity for multiple values of each input. Because the precursors are present in very small quantities in a dilute state, the outputs (thickness and uniformity) are linear in terms of the precursors, although they are non-linear function of the temperatures.

The resulting static map relating the recipe variable set-points (inputs) to the corresponding sets of measured performance parameters (outputs) is called the response surface, and is represented by a $m \times n$ matrix, $P$, with $m$ being the number of outputs and $n$ the number of recipe variables. Each column of $R$ corresponds to a 10% perturbation in each of the $n$ inputs, while holding the other inputs at the nominal values. Inversion of this matrix is the key to run-to-run control. In this case, it is a 3×3 matrix. In general, there would be a limit to control accuracy if $n$ is much smaller than $m$, which is often the case. Controller accuracy may be improved by increasing $n$, e.g., by considering the temperatures of the three susceptor zones as inputs. The number and choice of manipulated inputs and measured outputs are important factors in achieving the desired control goals, and for determining if an "optimal" choice of controller is possible.

### 3.3 Run-to-Run Control

The goal of a manufacturing system is to produce multiple copies of the same product, each having properties within specified tolerances. Product quality properties are typically determined after the product is manufactured, since in most cases sensors are not available to directly monitor the properties during the process. Furthermore, the control (or recipe) variables are pre-set and remain unchanged. The run-to-run control problem is to adjust the recipe for the *next* run based on the results of the previous runs such that the product quality approaches the desired values.

The algorithm behind run-to-run control is relatively simple, and may be analyzed using standard control theory as described next [14]. Let $t = 1,2,....$, denote the run number, $r_t \in R^m$ the vector of recipe variables used during run $t$, $y_t \in R^n$ the vector of properties of the product produced at the end of run $t$, and $e_t$ denote the normalized product quality error, whose $i^{th}$ element is defined as,

$$e_t(i) = ( y_t(i) - y_{des}(i) ) / y_{tol}(i) \qquad i = 1,...,n \qquad (3)$$

Here $y_{des}$(i) is the $i^{th}$ desired property (e.g., average film thickness), and $y_{tol}$(i) is the associated error tolerance. The error, written in vector form, is

$$e_t = R^{-1}(y_t - y_{des})$$

$$R = \text{diag}\,(y_{tol}(1),...,y_{tol}(n)) \tag{4}$$

The simplest choice for run-to-run control is to correct the previous recipe input by an amount *proportional* to the current error. Thus, for run $t$ =1,2,…, the recipe variables are adjusted in the following way:

$$r_t = r_{nom} + u_t$$

$$u_t = u_{t-1} - \Gamma\, e_{t-1}, \qquad u_0 = 0 \tag{5}$$

Here $r_{nom}$ is the vector of nominal recipe values, $u_t$ is the *correction* to the nominal recipe for run $t$, and $\Gamma \in R^{mxn}$ is the control design (gain) matrix. It is emphasized that Equation sets (4) and (5) together constitute the *complete* run-to-run algorithm. It is also noted that Equation (5) has the same form as a gradient descent optimization algorithm. It is possible to choose Γ and to analyze the algorithm under a variety of assumptions about how $u_t$ effects $e_t$ [14]. It can be shown that most of the widely used run-to-run algorithms used in process control are identical to Equations (5) with different choices of the control design (gain) matrix Γ. The choice of Γ for this case is discussed in the next section.

### 3.4 Run-to-Run Control for MOCVD Process

The vector of output variables, $y$, is given below:

$$y = \begin{bmatrix} S_{Ba} \\ S_{Cu} \\ R_{av} \end{bmatrix} \tag{6}$$

Here, the stoichiometries are denoted by $S_{Ba}$ and $S_{Cu}$ and correspond to the molar ratios of BaO to $Y_2O_3$ and CuO to $Y_2O_3$ at the center of the wafer, respectively. $R_{av}$ denotes the average growth-rate in Å/min. The vector of recipe variables, $r$, is given by

$$r = \begin{bmatrix} Y \\ Ba \\ Cu \end{bmatrix} \tag{7}$$

Here, *Y, Ba* and *Cu* are the precursor masses expressed as fractions of the total gas mass entering the chamber. The desired film properties are generally specified in the form of acceptable range of the values of the outputs. In this case, we have chosen the following range:

$$\begin{aligned} 1.5 \le\ & S_{Ba} \le 2.0 \\ 3.0 \le\ & S_{Cu} \le 4.0 \\ 32 \le\ & R_{av} \le 40 \end{aligned} \tag{8}$$

For implementing run-to-run control, we need to specify a single operating point within the acceptable region, e.g.,

$$y_{des} = \begin{bmatrix} 1.6 \\ 3.2 \\ 35.0 \end{bmatrix} \tag{9}$$

The control problem here is to reach the region of acceptance defined in the set of Equation (8) starting from a nominal point [$r_{nom}$, $y_{nom}$] in as few iterations as possible.

Before employing Equations (4) and (5) for run-to-run control, we have to determine the 3×3 control design (gain) matrix gain, Γ. For this purpose we assume that the deposition process may be described by the following static linear error system:

$$e_t = w_t + G\,u_t \qquad t = 0,1,2,\ldots \tag{10}$$

Here, $G$ is a 3×3 matrix that relates changes in error due to changes in values of inputs, and is determined as follows:

$$G_t = P - [y_{nom}\,,\, y_{nom}\,,\, y_{nom}] \tag{11}$$

Also, $w_t$ is the vector of errors in product quality (thickness, stoichiometry) after run $t$ due solely to the nominal recipe variable settings, $r_{nom}$, i.e.,

$$w_t = e_t \,|_{\,r_t = r_{nom}} \tag{12}$$

The gain matrix, Γ, is obtained as

$$\Gamma = \mu\, G^{\dagger} \tag{13}$$

If $G$ is a square matrix, then $G^{\dagger} = G^{-1}$, or else

$$G^{\dagger} = G^{T}\,(G\,G^{T})^{-1} \tag{14}$$

In Equation (14), $G^{\dagger}$ is called the right pseudo-inverse of $G$. The gain factor, $\mu$, is a number between 0 and 1, and is used to trade-off speed of convergence *vs.* amplification of measurement noise. In theory, the system is stable for $0 < \mu < 2$ [14]. However, in practice, the iterations may diverge for $\mu$ as small as unity if the nominal operating point is far away from the target operating point. In such situations, the run-to-run gains are large, because they are based on a large error, and result in instability. Smaller values of $\mu$ leads to convergence although the number of iterations increases. For a linear model input-output model as this, the computer iterations are almost instantaneous, and a large number of iterations do not pose any problem.

For a highly non-linear model, even a locally non-linear response surface model may be inadequate for the process to reach the target operating region if the starting point is far away. However, it is not practical to do experiments (i.e., either process actual wafers or run a very accurate high-order CFD-ACE™ model that is computationally intensive) for each of the several dozen iterations. We therefore propose the following four-step approach for such cases.

1. Identify run-to-run gain in nominal (current) operating point from experiments.
2. Simulate a run-to-run iteration with an approximate (linear or locally non-linear) response surface model using a low value of $\mu$ and iterate sufficiently so as to converge with high accuracy to the desired operating point.

3. Use this optimal simulated input values obtained in step 2 as a starting point for a new experiment. Determine to what extent the measured performance differs from the optimal simulated performance.
4. If the performance falls outside the target region, identify new run-to-run gains for the new operating point – which should be much closer to the target operating point – and repeat steps 2 and 3 until acceptable performance is achieved.

The above method combines fast computer simulations with a minimal number of experiments to bring a process back to within specifications following a relatively large disturbance.

After determining $\Gamma$, and with an appropriate choice of $\mu$, Equations (5) and (10) are used to determine the set-points of the recipe variables for the next run, $r_t$. In our case, we start with the following nominal recipe, $r_{nom}$.

$$r_{nom} \doteq \begin{bmatrix} Y_{nom} \\ Ba_{nom} \\ Cu_{nom} \end{bmatrix} = \begin{bmatrix} 0.00281019 \\ 0.00287371 \\ 0.00032728 \end{bmatrix}.$$

The corresponding nominal performance variables were computed as:

$$y_{nom} \doteq \begin{bmatrix} S_{Ba}^{nom} \\ S_{Cu}^{nom} \\ R_{av}^{nom} \end{bmatrix} = \begin{bmatrix} 1.80 \\ 3.27 \\ 46.7 \end{bmatrix}$$

This resulted in the following gain matrix:

$$\Gamma = \mu \begin{bmatrix} 1.27741 & 0.589299 & -0.136576 \\ -2.17384 & 0.537086 & -0.124475 \\ 1.1866 & -1.32447 & -0.126867 \end{bmatrix}.$$

To test how well the run-to-run control scheme works for this MOCVD process, we start at a point very far from the target area with $r_0$ and $y_0$ given by:

$$r_0 = \begin{bmatrix} 0.01 \\ 0.0008 \\ 0.0002 \end{bmatrix}, \qquad y = \begin{bmatrix} 0.14 \\ 0.06 \\ 61.5 \end{bmatrix},$$

Using ternary diagrams, Figure 14 and 15 show run-to-run iterations for $\mu = 0.6$ and $\mu = 0.8$, respectively. The target region described by Equation (8) is shown as a quadrilateral in the ternary diagrams. Starting from the yttrium-rich region of the diagram, the iterative cycle with $\mu = 0.6$ converges in twenty iterations. The iterative cycle with $\mu = 0.8$ does converge in fewer (seventeen) iterations, but is almost unstable. Larger values of $\mu$ indeed cause the iteration to diverge. Iterations with $\mu = 0.2$ (not shown) look similar to iterations with $\mu = 0.6$, except that fifty-seven iterations were needed to reach the target point. Since these simulations are done on computer, it is immaterial as to which value of $\mu$ we use, as long as the iterations converge. However, if an actual experiment were performed for every iteration, then it would be desirable to use the largest value of $\mu$ that is stable. The following recipe are obtained with $\mu = 0.6$ after full convergence to the desired output, $y_{des}$:

$$r^{20}_{\mu=0.6} = \begin{bmatrix} 0.00220979 \\ 0.00200987 \\ 0.00251877 \end{bmatrix},$$

Using the new inputs, we recomputed the nonlinear CFD-ACE™ simulation to check how much the 'experimental' results would differ from the approximate solution. The resulting performance variables were given by:

$$y = \begin{bmatrix} 1.60 \\ 3.21 \\ 35.1 \end{bmatrix},$$

These values are very close to the desired values of $y_{des}$ (Equation 9). This accurate convergence was achieved because the thickness and stoichiometry are very linear in terms of the precursor mass fractions. Since the uniformity is very good, the film properties within the entire wafer are within specifications.

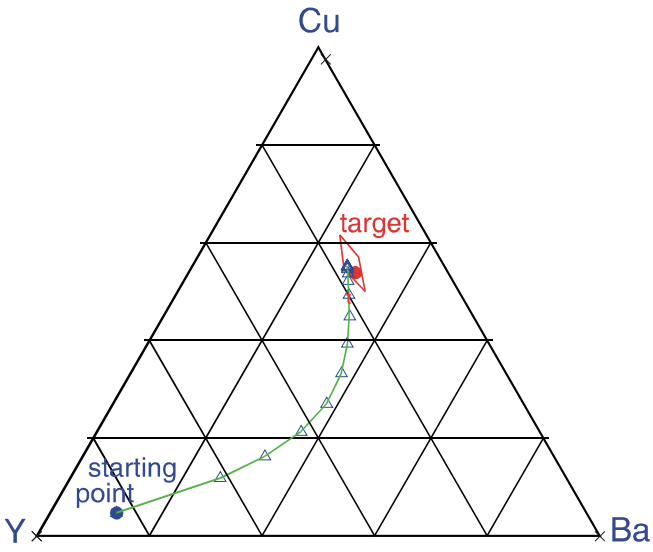


**Figure 14.** Ternary diagram showing twenty run-to-run iterations from the starting point to the target operating point using $\mu$ = 0.6. The starting point and target point are shown using bullets, while the individual iterations are shown as small triangles. The desired operating area is shown as a quadrilateral.

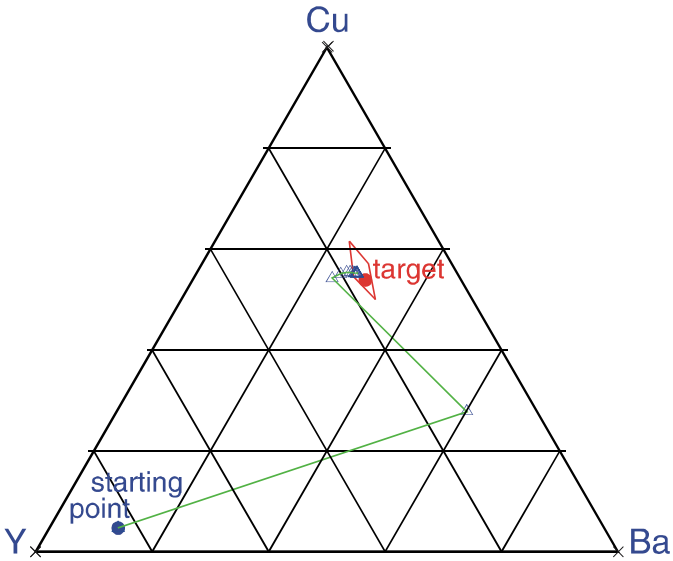


**Figure 15.** Ternary diagram showing seventeen run-to-run iterations from the starting point to the target operating point using $\mu$ = 0.8. The starting point and target point are shown using bullets, while the individual iterations are shown as small triangles. The desired operating area is shown as a quadrilateral.

The implication of this result is significant because it indicates that it is possible to speed up the run-to-run control by performing the iterations on a virtual reactor in simulation, and performing experiments only to test the accuracy of the converged values of thickness and stoichiometry. The use of model-based simulations for run-to-run control significantly reduces the cost associated with the use of actual wafers and increases throughput while improving reproducibility. Even if the run-to-run control cannot provide the desired stoichiometry after the first set of iterations, the new starting point as determined from the experiments will be much closer to the target region than would otherwise be possible.

## 4 Conclusions

A reactor-scale physical model for MOCVD of YBCO was developed. The model includes chemical kinetics and species transport to the wafer surface. The YBCO deposition rates obtained from these simulations are comparable to those published in the literature. Sensitivity calculations using this model were used for run-to-run controller design. A general control structure was developed for MOCVD reactor control. An innovative run-to-run control method was developed which enables efficient stoichiometry control. In practice, a wafer would be processed, and performance measures (average film thickness and stoichiometry) would be determined using *ex-situ* metrology. The run-to-run control iterations would then be run on the virtual reactor on computer to determine adjustments to the values of the recipe variables for the next wafer run in order to reach the desired stoichiometry region. Application of run-to-run control enables the tolerance band around the desired product property values to remain narrow. Additionally, the process can return very quickly to the region within the tolerance band after a large disturbance or following process start-up wasting a minimal number of wafers in the process.

**Acknowledgements:**

This work was supported by the Defense Advanced Research projects Agency (DARPA)'s Applied Computational Mathematics program under the Office of Naval Research Contract N00014-98-C-0201. The authors would also like to acknowledge the help of CFD Research Corporation (CFDRC) of Huntsville, AL.

# References:

[1] K. F. Jensen, in *Handbook of Crystal Growth*, Vol. 3 Part B, edited by D. T. J. Hurle (Elsevier, Amsterdam, 1994), pp. 593.

[2] W. R. Rees, *CVD of Non-Metals* (VCH, Weinhem, 1993).

[3] K. H. Dahmen and T. Gerfin, Prog. Cryst. Growth Char. **27,** (1993) p. 117.

[4] M. Leskela, H. Molsa, and L. Niinisto, Superconductor Science and Tecnology **6,** (1993) p. 627.

[5] I. M. Watson, Chem. Vap. Depos. **3,** 1 (1997) p. 9.

[6] K. Kanehori, N. Sughi, T. Fukazawa, and K. Miyauchi, Thin Solid Films **182,** (1989) p. 265.

[7] H. Yamanae, M. Hasei, H. Kurosawa, and T. Hirai, Jap. J. Appl. Phys. **30,** 6A (1991) p. L1003.

[8] *CFD-ACE+™ Manuals* (CFD Research Corporation, Huntsville, AL, 2000).

[9] J. P. van Doormal and G. D. Raithby, Numerical Heat Transfer **7,** (1984) p. 147.

[10] L. L. Raja, R. J. Kee, R. Serban, and L. R. Petzold, J. Electrochem. Soc. **147,** 7 (2000) p. 2718.

[11] L. L. Raja, Colorado School of Mines, private communication, (2000)

[12] R. B. Bird, W. E. Stewart, and E. N. Lightfoot, *Transport Phenomena* (Wiley, New York, 1960).

[13] F. Schmaderer and G. Wahl, Journal de Physique C5 (1989) p. 119 .

[14] R. Kosut, D. D. de Roover, A. Emami-Naeini, and J. L. Ebert, in *Proc. 37th IEEE Conf. Decision Control* (December 1998).